Experimental Methods for Measuring Elasto-plastic Parameters of Bentonite Clay

Aaro Eloranta

Master's Thesis
University of Jyväskylä
Department of Physics
May 8, 2012
Advisor: Markku Kataja

Acknowledgements

I would like to thank the following persons for their continued help and support during my work on this thesis and during my years at the University of Jyväskylä

- *Markku Kataja* for his expert help and advice.
- *Jarno Alaraudanjoki* for his patient help on numerous technical matters.
- *Tero Harjupatana* for peer support and his sense of humor in the lab.
- *The staff of the workshops of University of Jyväskylä* for their irreplaceble help and for answering numerous dumb questions with considerable patience.
- *My fellow students*, for their invaluable support, laughter and company during our years at our department.
- *My friends and family (especially Mum)* for their continuing love and support.
- *My science and math teachers in primary and high school as well as at the university* for making it possible for me to appreciate the beauty and wonder of science.

Abstract

This thesis presents the results for experiments in which elasto-plastic deformation properties of purified bentonite clay were investigated in constrained one-dimensional and hydrostatic compressions. The one-dimensional compression experiments were carried out by compressing uncompacted purified bentonite between two sintered surfaces inside a closed chamber. The hydrostatic compression experiments were carried out by enveloping a compacted bentonite sample with a thin shell of rubber and compressing the sample in pressurized water.

The main objective was to test and improve experimental methods for measuring the deformation properties of bentonite clay. The second objective was to produce data that can be used to validate deformation models for purified bentonite clay. It was assumed that the bentonite follows the isotropic linear elasticity theory for small deformations when the deformations are elastic.

The yield limit in hydrostatic compression was so high that it was not possible to cause significant plastic deformation using pressures between 0 and 10 MPa, that the current device is designed for. For this reason it was not possible to determine the yield limit in hydrostatic compression.

The one-dimensional compression experiments succeeded well. Based on the results, the shear modulus G as a function of the Poisson ratio ν, water content η and dry density ρ_0 (see equations (2.13) and (2.10) for the definitions) was calculated. The results agreed well with an equation of functional form

$$G(\rho_0,\eta,\nu) = \frac{1-2\nu}{2(1-\nu)}\left[(a+b\eta)\left(\frac{\rho_0}{c-\rho_0}\right)+d\right].$$

The yield limit p_{yield} in one-dimensional constrained compression agreed with an equation of functional form

$$p_{\text{yield}}(\rho_0,\eta) = a_1 + a_2\rho_0 + a_3\eta + a_4\rho_0^2 + a_5\rho_0\eta + a_6\eta^2.$$

Based on results from both compression experiments, it was estimated that for bentonite clay with dry density $\rho_0 \geq 1.47\,\mathrm{g\,cm^{-3}}$ and water content $\eta \in [0.07, 0.25]$ the Poisson ratio was

$$0.42 \leq \nu \leq 0.50.$$

See section 4.5 for all numerical results and Chapter 5 for discussion about the development of the experimental methods.

Tiivistelmä

Tässä pro gradu -tutkielmassa esitetään kokeellisia tuloksia puristuskokeista, joissa tutkittiin puhdistetun bentoniittisaven elasto-plastisia muodonmuutosominaisuuksia. Puristuskokeita oli kahdenlaisia. Yksiulotteisissa puristuskokeissa aiemmin puristamatonta bentoniittia puristettiin suljetussa kammiossa kasaan kahden teräksisen sintteripinnan välissä. Hydrostaattisissa puristuskokeissa aiemmin kokoonpuristettuja ohuella kumikerroksella päällystettyjä bentoniittinappeja puristettiin kasaan paineistetun veden avulla.

Työn ensisijainen tarkoitus oli kokeilla ja kehittää kokeellisia menetelmiä bentoniittisaven muodonmuutosten tutkimista varten. Toissijainen tavoite oli tuottaa mitattua tietoa puhdistetun bentoniitin laskennallisten muodonmuutosmallien varmentamiseksi. Työssä oletettiin, että bentoniitin elastiset muodonmuutokset noudattivat isotrooppista pienten muodonmuutosten elastisuusteoriaa.

Bentoniittinäytteiden myötöraja hydrostaattisessa puristuksessa oli niin korkea, että näytteitä ei saatu merkittävästi myötämään paineen arvoilla 0–10 MPa. Laitetta ei ole suunniteltu kestämään tätä suurempaa painetta. Tästä syystä kokeissa ei onnistuttu määrittämään puhdistetun bentoniitin myötörajaa hydrostaattisessa puristuksessa.

Yksiulotteiset puristuskokeet onnistuivat hyvin. Siitä saatujen tulosten perusteella laskettiin bentoniitin liukukerroin G Poisson-suhteen ν, kuivatiheyden ρ_0 ja kosteuden η funktiona (suureiden määritelmät löytyvät yhtälöistä (2.13) ja (2.10)). Tulokset ovat sopusoinnussa yhtälön kanssa, jonka muoto on

$$G(\rho_0,\eta,\nu) = \frac{1-2\nu}{2(1-\nu)}\left[(a+b\eta)\left(\frac{\rho_0}{c-\rho_0}\right)+d\right].$$

Myötöraja p_{yield} yksiulotteisessa puristuksessa noudatti likimain yhtälöä, joka on muotoa

$$p_{\text{yield}}(\rho_0,\eta) = a_1 + a_2\rho_0 + a_3\eta + a_4\rho_0^2 + a_5\rho_0\eta + a_6\eta^2.$$

Molempien kokeiden perusteella arvioitiin, että Poisson-suhde bentoniitille, jonka tiheys on $\rho_0 \geq 1.47\,\mathrm{g\,cm^{-3}}$ ja jonka kosteus on välillä $\eta \in [0.07, 0.25]$, oli

$$0.42 \leq \nu \leq 0.50.$$

Kaikki numeeriset tulokset on koottu osioon 4.5 ja yhteenveto kokeellisten menetelmien kehityksen tämänhetkisestä tilanteesta on luvussa 5.

Contents

1 Introduction

Bentonite is a common name for certain types of clay minerals. For most types of bentonite, the main mineral ingredient is montmorillonite, which belongs to the smectite mineral group. Because of its unique rheological properties, there are plans to use bentonite clay as a barrier material in final deposition of spent nuclear waste. [1]

Because the timescales involved in nuclear waste deposition are very long, direct experiments in this time scale are not feasible. Instead, safety and performance analysis of different deposition solutions must be based on computer simulations and different experimental studies. Experiments carried out in laboratory conditions can provide crucial information for testing and refining the computational models used in safety assessment of different solutions.

The main objective of this thesis was to test and improve experimental methods for investigation of the stress-strain behavior of bentonite clay. The secondary objective was to provide data for validation of different computational models of deformation for purified bentonite clay, particularly for the related x-ray tomography studies at the University of Jyväskylä.

In the experiments purified bentonite clay was compressed in cyclic hydrostatic and constrained one-dimensional compressions. It was assumed that the bentonite obeys the isotropic linear elasticity theory when the deformations are elastic. The measured quantities were the elastic bulk modulus K, the elastic p-wave modulus M and the yield limit in both types of compression. Based on these results, estimates for the Poisson ratio ν and shear modulus G of the purified bentonite were found.

Chapter 2 explains briefly the theoretical basis of the experimental work and introduces some definitions used in later chapters. Chapter 3 describes the experimental methods used. Chapter 4 details the observations and data analysis, and summarizes the results. Finally, Chapter 5 summarizes and discusses the current status in the development of the experimental methods used in this thesis.

2 Theory of deformation of clay

2.1 Elasticity and plasticity

Deformation theory aims to describe the behavior of condensed matter when the matter is loaded either mechanically or thermally. When external forces are applied to a body, the shape or size of the body may change. The goal is to relate these changes to the applied forces.

Any state of the body can be taken as the *reference state*, against which all changes are measured. Similarly, the external conditions (e.g. applied forces) when the body is at its reference configuration are called the *reference conditions*. When the conditions change (e.g. the magnitude of loading forces increases), the body may undergo a deformation. If the body returns to the reference state when the external conditions are brought back to reference conditions, the deformation is called *elastic deformation*. [2]

If the change of conditions results in a lasting deformation which remains after the return to reference conditions, the remaining deformation is called *plastic deformation*. In many cases, the deformation of a physical body consists of both an elastic part and a plastic part. [2]

The physical foundation of plasticity of clay can be understood by examining the structure of claylike materials. Clay are granular materials and have varying amounts of space between individual grains. These spaces or pores are typically filled with water or air or some mixture of both. [3]

Compression of clay affects the positioning between grains, typically reducing the total volume of the pores and thus causing irreversible plastic deformations. Deformations of individual grains can also take place, especially at high pressures or when the grains have been softened by moisture. Bentonite contains significant amounts of absorbed water under many circumstances. The amount of water absorbed by bentonite significantly influences the deformation properties of the bentonite.

2.2 Strain and stress

The deformation of a body and the forces applied to it are described by tensor quantities called *strain* E and *stress* σ. The body is modeled as a continuous bulk of matter occupying a region $R \subset \mathbb{R}^3$ in its reference state. When the body is deformed, every point of the material $\vec{r}_0$ is moved to another point $\vec{r}$ as described by the *displacement vector*

$$\vec{u}(\vec{r}_0) = \vec{r} - \vec{r}_0.$$

However, the displacement vector does not adequately describe the deformation of the body, since it does not express the displacement of the points relative to each other. The proper measure of deformation is the strain tensor E. The components of this 2nd rank tensor in a cartesian coordinate system (x_1,x_2,x_3) are

$$E_{ij}(\vec{r}_0) = \frac{1}{2}\left(\frac{\partial u_j}{\partial x_i} + \frac{\partial u_i}{\partial x_j} + \sum_{k=1}^{3} \frac{\partial u_k}{\partial x_i}\frac{\partial u_k}{\partial x_j}\right). \tag{2.1}$$

Strain E describes the deformation of an infinitesimal neighborhood of $\vec{r}_i$. [2]

If all of the partial derivatives in (2.1) are sufficiently small, the last term can be omitted and the strain tensor E can be approximated with the *infinitesimal strain tensor* ϵ:

$$E_{ij}(\vec{r}_0) \approx \epsilon_{ij}(\vec{r}_0) = \frac{1}{2}\left(\frac{\partial u_j}{\partial x_i} + \frac{\partial u_i}{\partial x_j}\right). \tag{2.2}$$

Such deformations can be referred to as either *small or infinitesimal deformations*. Note that here both strain tensors are presented as functions of the reference state points $\vec{r}_0$. This approach is called the Lagrangian approach. For the other, the so called Eulerian approach, see for example [2]. The Lagrangian and the Eulerian approaches give identical results for small deformations. [2]

The forces acting on the body can be divided into *body forces* (e.g. gravity) acting on all points of the body and *surface forces* that act on the surface of the body. Often, the only significant body force is gravity. In the deformations discussed in this thesis, the effect of gravity is very small compared to the effect of the surface forces, so the effect of body forces is neglegted.

The surface forces are described by the stress tensor

$$\sigma = \begin{pmatrix} \sigma_{11} & \sigma_{12} & \sigma_{13} \\ \sigma_{21} & \sigma_{22} & \sigma_{23} \\ \sigma_{31} & \sigma_{32} & \sigma_{33} \end{pmatrix}. \tag{2.3}$$

The stress tensor is symmetric and expresses the magnitude of various types of contact forces per unit of surface area. The forces can be thought as acting on the surfaces of an infinitesimal rectangular volume with side lengths $\mathrm{d}x_1$, $\mathrm{d}x_2$ and $\mathrm{d}x_3$. The stress element σ_{ij} describes the magnitude per area of the force component F_j on surface perpendicular to coordinate axis x_i. The diagonal elements σ_{ii} (no sum) represent forces that try to compress or stretch the volume in direction of x_i, while the off-diagonal elements represent shearing forces. [2][4]

Like any other symmetric 2nd rank tensor, the stress tensor can be diagonalized in all points. This diagonalizing corresponds to a rotation of the original coordinate axes to a new set of axes (x_1^*,x_2^*,x_3^*). In this coordinate system the representation of the stress tensor is a diagonal matrix

$$\sigma^* = \begin{pmatrix} \sigma_1 & 0 & 0 \\ 0 & \sigma_2 & 0 \\ 0 & 0 & \sigma_3 \end{pmatrix}. \tag{2.4}$$

The stresses σ_i are called the *principal stresses* at that point. The new set of coordinate axes (x_1^*,x_2^*,x_3^*) is called the *principal axes of stresses.* [2][5]

2.3 Isotropic linear elasticity

The most simple model of elastic behavior is called isotropic linear elasticity. This model assumes that

- strains are sufficiently small for equation (2.2) to be valid
- material is homogenous and isotropic
- temperature is approximately constant
- all stresses are linear functions of strains, i.e. there is a 4th rank tensor C so that $\sigma_{ij} = \sum_{k,l=1}^{3} C_{ijkl}\epsilon_{kl}$.

These assumptions combined with the symmetry of the stress tensor lead to equation

$$\sigma_{ij} = \lambda\delta_{ij}\sum_{k=1}^{3}\epsilon_{kk} + 2\mu\epsilon_{ij}, \tag{2.5}$$

where material dependent parameters λ and μ are called the *Lamé coefficients.* [2]

It is difficult to directly determine the Lamé coefficients experimentally. However, if the material is easy enough to compress, it is straightforward to calculate them from directly measurable quantities such as the *bulk modulus* K and the *p-wave modulus* M. For nearly incompressible materials the changes in the volume and shape of the body may be too small to be measured accurately.

The bulk modulus can be measured by compressing the body hydrostatically ($\sigma = \mathrm{diag}(-p, -p, -p)$, where p is the pressure) and using the equation

$$K = -V\frac{dp}{dV}, \tag{2.6}$$

where V is the volume of the body. [4]

Similarly, the p-wave modulus can be measured in a one-dimensional constrained compression test as

$$M = -h\frac{dp_1}{dh}, \tag{2.7}$$

where h is the height of the body in the direction of compression and p_1 is the loading pressure applied to the body. [4]

In the linear isotropic elasticity theory the changes in volume and height are infinitesimal. For this reason, the volume and height are effectively constant. The changes measured in this work are finite, however. To use the theory of linear isotropic elasticity the values of height and volume in equations (2.6) and (2.7) were assumed to be constant during the elastic deformations. To avoid any confusion, these constant values are called the *elastic reference volume and height*, respectively.

These moduli are related to the Lamé coefficients by following equations: [4]

$$\lambda = \frac{1}{2}(3K - M)$$
$$\mu = \frac{3}{4}(M - K).$$

Thus the elastic deformation parameters for an isotropic body at constant temperature for small deformations can be acquired by measuring the bulk modulus and p-wave modulus of the body.

Other parametrisations and their relations to the measured moduli can also be used to express the results. The Poisson ratio ν can be calculated from M and K with equation [4]

$$\nu = \frac{3K - M}{M + 3K}. \tag{2.8}$$

The Poisson ratio is between 0 and 1/2 for most materials.[1] [4] The shear modulus G can be written in terms of M and ν as

$$G = \frac{1 - 2\nu}{2(1 - \nu)}M. \tag{2.9}$$

2.4 Yielding and yield surface

Most deformations remain elastic as long as the applied stresses are sufficiently small. If the stresses grow sufficiently large, at least a part of

[1] For some rather exotic materials, the Poisson ration can be negative, but it is always between -1 and $1/2$. [4]

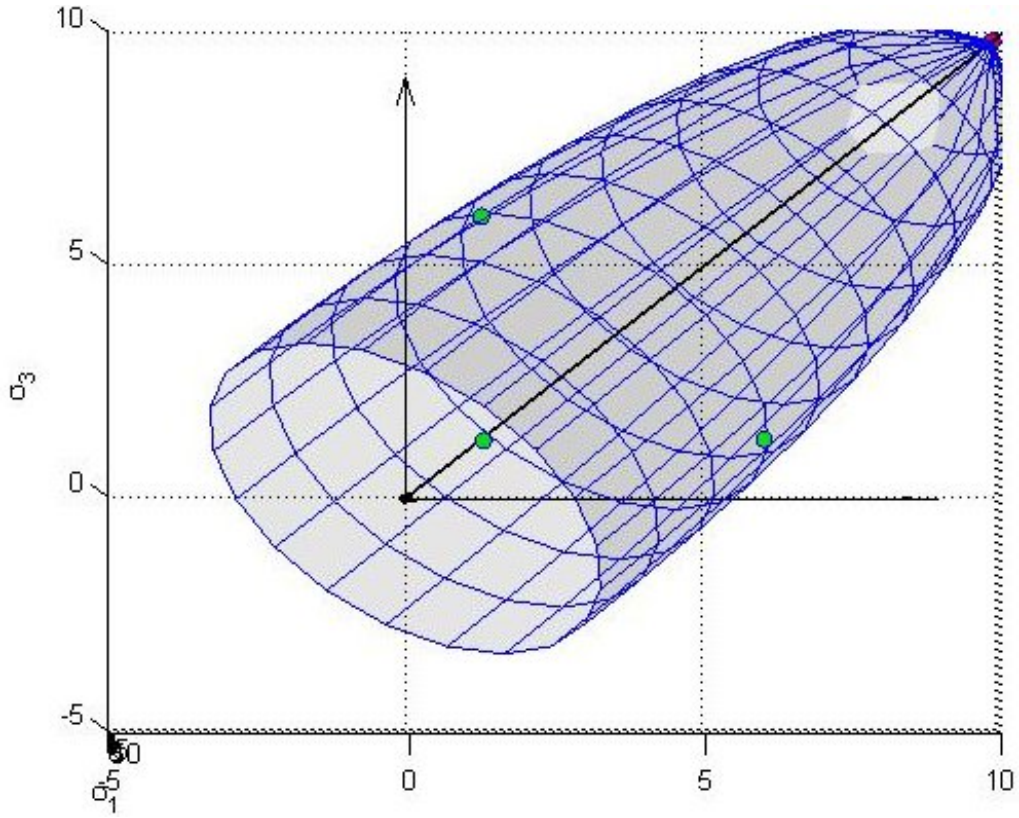

Figure 2.1: Example of a yield surface in the stress eigenspace. The depicted surface was obtained from preliminary experimental data by assuming the the yielding is described by modified von Mises yield criteria.

the accompanying deformation is plastic deformation. This phenomenon is called yielding, and the limiting stress at which plastic deformations begin to take place is called yield point or yield limit.

Equation (2.4) shows that after the principal axes of stresses at a certain point are determined, the principal stresses can unambiguously describe the stress state at that point. It's therefore useful to describe the stress state as a point in a three dimensional *$(\sigma_1, \sigma_2, \sigma_3)$ -stress eigenspace.*

The limiting stress states where plastic deformations begin to take place are described by a contour surface of the yield function $f(\sigma_1, \sigma_2, \sigma_3)$. This contour surface in the stress eigenspace is called the *yield surface.* For an example of a yield surface, see figure 2.1. There are many different yield functions based on different assumptions and yield criteria. Some yield functions describe the behavior of some materials better than others, but no single function can be considered universally better than others. [6]

The experiments detailed in this thesis give information on the location of two points of the yield surface of the bentonite. These points are the yield point in hydrostatic compression and the yield point in one-dimensional constrained compression. In the first case all principal stresses are equal and in the second their relative magnitudes depend on the Poisson ratio of the material. The Poisson ratio in turn can be calculated from the measured bulk modulus and p-wave modulus. The determination of the location of these two points in the stress space provides a starting point for modeling the entire yield surface of the bentonite. [4]

2.5 Typical loading curves of clay

In this thesis, *compression pressure* will mean either the hydrostatic pressure p when discussing hydrostatic compression or the loading pressure p_1 in one-dimensional compression. When clay is compressed cyclically so that the compression pressure increases on every new compression, the resulting loading-unloading curve resembles the curve in figure 2.2. The shape of the curve is similar both in one-dimensional and hydrostatic compressions. The maximum pressure that has been previously applied to the clay sample is called *consolidation pressure*. [3]

The yield limit of a clay sample is approximately equal to the consolidation pressure. If the sample is loaded with compression pressure greater than consolidation pressure, plastic deformations take place. When the sample is unloaded, the volume or height of the sample does not return to its previous value (see the loops in figure 2.2). The new consolidation pressure is now the yield limit of the sample. When the sample is loaded again, the deformation remains elastic as long as the pressure does not exceed the new yield limit, but if it is exceeded, further plastic deformation takes place. The curve that describes the behavior of the sample during the plastic deformations is called *the virgin curve*. [3]

While the strain-stress curve is not exactly linear in the elastic region, it is convenient and often sufficient to model it as such. This means using linear elasticity theories. In this thesis the elastic deformations were assumed to obey the linear isotropic homogenous elastic model described in section 2.3. [3]

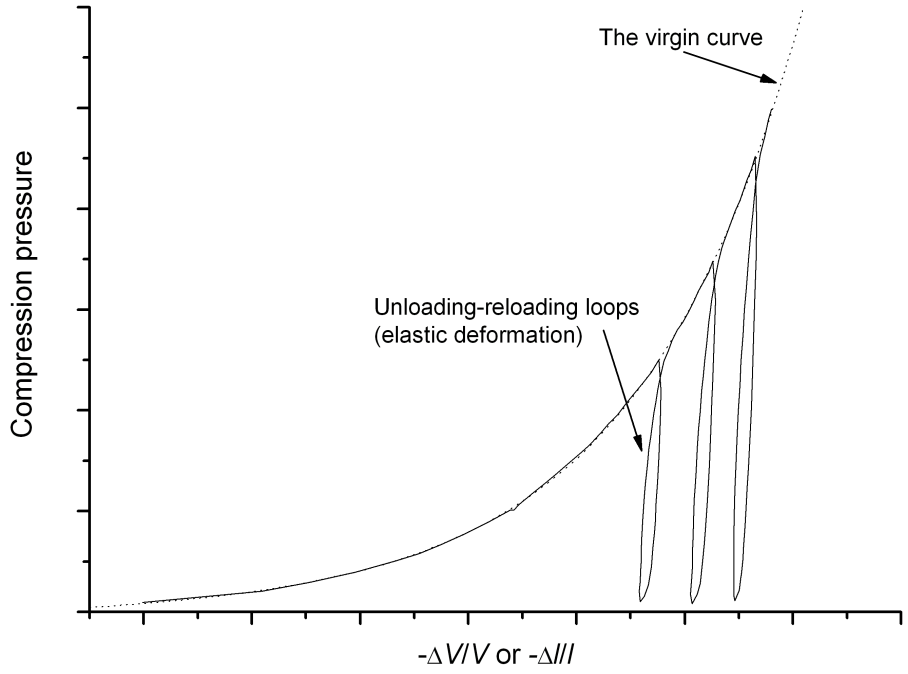

Figure 2.2: Qualitative graph showing the cyclic loading-unloading curve of a clay or claylike material in one-dimensional or hydrostatic compression. The vertical axis is the loading pressure and the horizontal axis is either the relative change in sample height (one-dimensional compression) or the relative change in sample volume (hydrostatic compression). The figure is adapted from [3].

2.6 Water content of bentonite clay

The amount of moisture greatly affects the stress-strain behavior of bentonite. Bentonite stored in room temperature and humidity also contains significant amounts of water. A quantity called *water content* was used to measure the humidity of the bentonite. Water content η is defined as the ratio of water mass and dry mass of the bentonite

$$\eta = \frac{m_{\text{water}}}{m_{\text{dry mass}}}. \tag{2.10}$$

With this definition, the masses of water and dry material in a bentonite sample with total mass $m_{\text{bentonite}}$ and water content η can be calculated

from equations

$$m_{\text{dry mass}} = \frac{m_{\text{bentonite}}}{\eta + 1} \tag{2.11}$$

$$m_{\text{water}} = \frac{\eta}{\eta + 1} m_{\text{bentonite}}. \tag{2.12}$$

Dry density ρ_0 is defined as the ratio between dry mass and sample volume

$$\rho_0 = \frac{m_{\text{dry mass}}}{V}. \tag{2.13}$$

Dry density is used to compare the behavior of samples with different water content. Combining the definitions (2.10) and (2.13) the relation between dry and actual densities of bentonite becomes

$$\rho_0 = \frac{\rho}{1 + \eta}, \tag{2.14}$$

where ρ is the density of the bentonite.

In terms of directly measurable quantities, the initial dry density of a sample in hydrostatic measurements described in this thesis is

$$\rho_0 = \frac{m}{(1 + \eta)\pi h r^2}, \tag{2.15}$$

where m, h and r is the mass, height and bottom radius of the sample, respectively. A similar equation

$$\rho_0 = \frac{m}{(1 + \eta)\pi h R^2}, \tag{2.16}$$

where $R = 4.5\,\text{cm}$ is the radius of the bottom of the compression chamber of the one-dimensional compression device, was used to calculate the dry density of samples in one-dimensional compression.

3 Experimental Methods

3.1 Controlling the water content of the samples

To determine the chemical composition of the purified bentonite, a chemical analysis was performed by Mia Tiljander at the Geological Survey of Finland. The analysis showed that the material was 90 ± 5 mass percent montmorillonite and 5 ± 5 mass percent quartz.

The water content of bentonite was measured by drying the bentonite in an oven as follows: First, the vessel to be used for drying the bentonite was kept in the oven at 105 °C until the mass of the vessel did not change anymore. Second, about 10 g of bentonite was weighted and laid in the vessel as flatly as possible. Finally, the bentonite was kept in the oven at 105 °C until its mass remained constant for at least half an hour. The difference between the final and initial masses was then used to calculate the water content. The drying vessel was so flat that the bentonite formed only a very thin layer on the bottom of it. The water content of bentonite stored in the laboratory was measured to be

$$\eta_0 = 0.0755 \pm 0.0017. \tag{3.1}$$

The value expressed in equation (3.1) was obtained as a weighted average from three separate measurements which agreed with each other within error limits.

The water content of bentonite was increased by mixing bentonite and water in a blender (see figure 3.1). The blender had a hole in its cover through which water could be added. For the remainder of this work, the bentonite that was moistened at the same time are said to form a patch of bentonite. By measuring the masses of the room-stored bentonite and added water, it was possible to determine the water content of each bentonite patch. Since some of the material unavoidably stuck in the walls and other parts of the blender, some mass loss was inevitable. Another source for lost mass is the evaporation of water. The blender heats up during the mixing, which may cause significant evaporation.

Because the amount of clay that remained in the blender was relatively small, a relatively small error occurs if it is assumed that all of the mass lost during mixing was water. The water content after mixing was estimated with this assumption by combining equations (2.10), (2.11) and (2.12) to

Figure 3.1: The primary equipment used in adding and mixing water with the clay.

equation

$$\eta = \frac{\eta_0 m_{\text{bentonite}} + (\eta_0 + 1)(m_{\text{water added}} - m_{\text{loss}})}{m_{\text{bentonite}}}, \tag{3.2}$$

where $m_{\text{bentonite}}$ is the mass of the bentonite including the initial water mass,

$m_{\text{water added}}$ is the mass of water added and m_{loss} is the total mass lost during the mixing.

Since equation (3.2) provides only an estimate for the water content, the water content of each patch of bentonite was measured twice after the water distribution process. These water content measurements for each patch were made just before making the first sample and just after all compression experiments had been completed. See section 4.1 for details and error analysis.

After mechanical mixing the distribution of water in the bentonite was uneven. To distribute the water evenly and to prevent evaporation, the bentonite was sealed into a plastic bag and left there for at least a week before making samples. During this week the bentonite was frequently stirred without opening the bag in order to speed up the water distribution process. Any visible large clumps were also smashed into smaller fragments when found.

The blender was so large that it was possible to moisten several hundred grams of bentonite at once. Hence it was possible to make several samples for both types of experiments from the same patch of moistened clay. There should not be significant differences in the water content of samples made from the same patch.

3.2 One-dimensional constrained compression

In the one-dimensional compression experiments previously uncompacted bentonite was compacted in cyclic constrained compression. The approximate turning point pressures used were 2 MPa, 4 MPa, 7 MPa, 9 MPa and 10 MPa The experimental set-up is depicted in figures 3.2 and 3.3. Bentonite was compressed by changing the volume of a compression chamber with a hydraulic pump. The bottom and top surfaces of the compression chamber were made of sintered steel surfaces, which allowed air to exit the chamber. Three Sangamo position sensors placed symmetrically around the chamber were used to measure the height of the sample. The average of the position sensor values was taken to be the actual height of the sample. The loading pressure was measured indirectly by measuring pressure in the hydraulic chamber with a Keller Leo 3 max. 300 bar pressure sensor.

The signals of the position and pressure sensors were transferred to a computer via a National Instruments DAQPad-6052E data acquisition card. The measurements were controlled with a LabView virtual instrument. The virtual instrument also compensated for the stretching of the compression device (see section 4.2) and calculated the density of the sample from mea-

sured height and bentonite mass. Further analysis of the data was done with Matlab scripts.

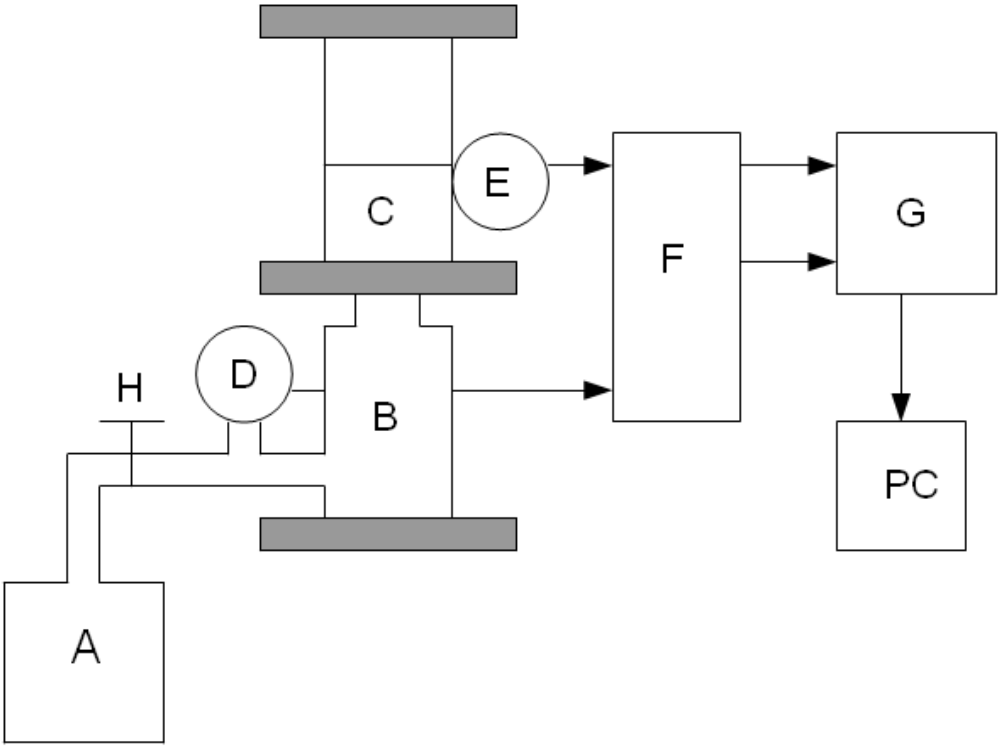

Figure 3.2: A schematic showing the experimental set-up and data acquisition in one-dimensional compression experiments. The letters denote the following components: **A** is the hydraulic pump, **B** is the hydraulic cylinder, **C** is the compression chamber, **D** is the pressure sensor, **E** denotes the position sensors, **F** is a connection box, **G** is the data acquisition card, **H** is a needle valve and **PC** is the computer.

Figure 3.3: The compression device for the one-dimensional constrained compression experiments. The letters refer to the same components as depicted in figure 3.2.

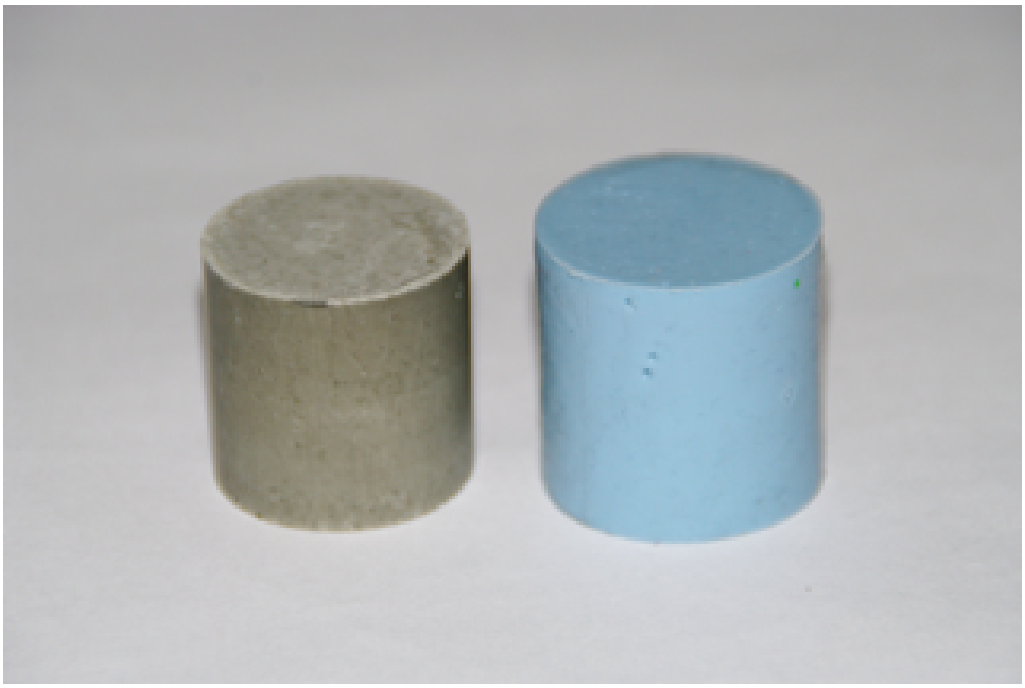

Figure 3.4: A photo showing an uncoated (left) and a rubber-coated sample (right).

3.3 Hydrostatic compression

Sample preparation

In the hydrostatic compression experiments the bentonite clay was compressed in pressurized water. Since adding moisture to bentonite clay greatly affects its deformation properties, the samples needed to be isolated from the water. This was accomplished by compacting clay into cylindrical samples and enveloping them with a thin coating of rubber. The details of sample preparation are described in [7].

Figure 3.4 shows a photo of an uncoated and a coated sample. The sample preparation method produced compacted clay cylinders with following approximate characteristics:

$$\begin{aligned} \text{height } h &\approx 30\,\text{mm}, \\ \text{diameter } d &\approx 30\,\text{mm} \\ \text{volume } V &\approx 21.2\,\text{cm}^3 \\ \text{dry density } \rho_0 &\approx 1.48\,\text{g}\,\text{cm}^{-3}. \end{aligned}$$

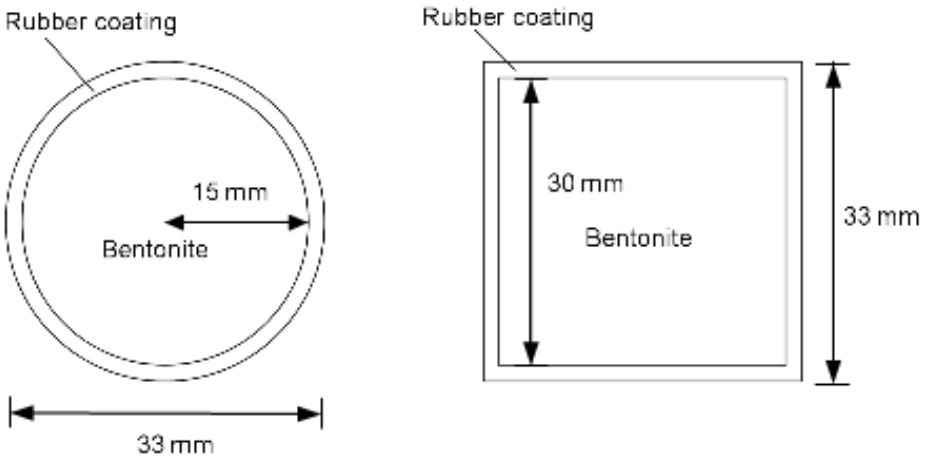

Figure 3.5: A diagram of the horizontal and vertical cross-sections of an ideal bentonite sample. In reality the clay may not lie perfectly straight inside the rubber. This is not a problem as long as the clay is isolated from the surrounding water during the experiments. The thickness of the rubber coating is not to scale.

The actual properties of each individual clay cylinder were measured with a scale and a caliper. The clay cylinder is enveloped with a rubber coating that is on average 1.5 mm thick. (See figure 3.5.) Small amounts of air bubbles got stuck within the rubber, but their effect was assumed negligible.

All hydrostatic samples with a given moisture were made from same patch of bentonite, so their moisture contents were likely identical. The dry densities of different samples varied from sample to sample because each sample was made individually. The samples were considered sufficiently identical if their dry densities were in the range

$$\rho_0 \in [1.46\,\mathrm{g\,cm^{-3}}, 1.50\,\mathrm{g\,cm^{-3}}]. \tag{3.3}$$

Experimental set-up

Figure 3.7 shows a diagram for the experimental set-up and data acquisition in hydrostatic compression experiments. Figure 3.6 is a photo of the main device. When filling the device with ion-exchanged water, the water flows in through valve **I** and out through valve **K**. The prepared samples were placed in the sample chamber **G** and immersed in water. The outer valves **I** and **K** were closed. Then the sample was compressed with the hydraulic pump while measuring the pressure and the motion of the double acting cylinder piston. The latter was used to measure the change of volume of the sample.

Before starting the measurements it was necessary to remove all air from the 2nd chamber of the double acting cylinder. This was done by disassembling the cylinder and the reassembling it underwater. The measurements were prepared as follows: First the sample chamber was open and partially filled with water. Water was allowed to flow in and the valve **J** was opened and closed repeatedly to remove all air from inside it. Next, the sample was immersed in the sample chamber. Then the sample chamber was closed and water was made to flow through the system to remove all air from it. The

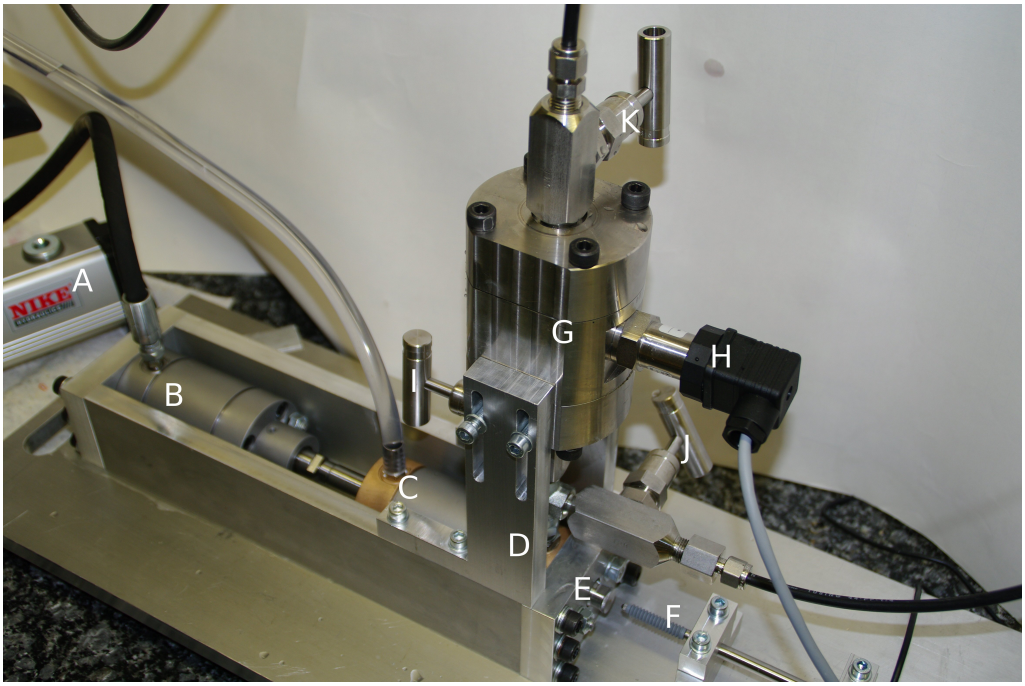

Figure 3.6: The compression device for the hydrostatic compression experiments. The numbers denote the same components as in figure 3.7.

upper valve was also opened and closed repeatedly to remove air bubbles. Finally the valves **I** and **K** were closed. Before each measurement the piston was moved to same position from the same direction to prevent changes in the position of the o-ring seal inside the double acting cylinder.

The measurements were cyclic compressions starting from ambient pressure with approximate turning point pressures 1.5 MPa, 2.5 MPa, 5 MPa, 7 MPa 9 MPa and 10 MPa. The pressure was measured with a Keller PA-25Y/200bar/80087.55 pressure sensor and the position with a position sensor. The data acquisition card was National Instruments cDaQ-9172. The measurements were controlled with a LabView virtual instrument. After the measurements the effect of the deformation of the device (see section 4.3) was subtracted from the measured changes in volume. Further analysis of the data was done with Matlab scripts.

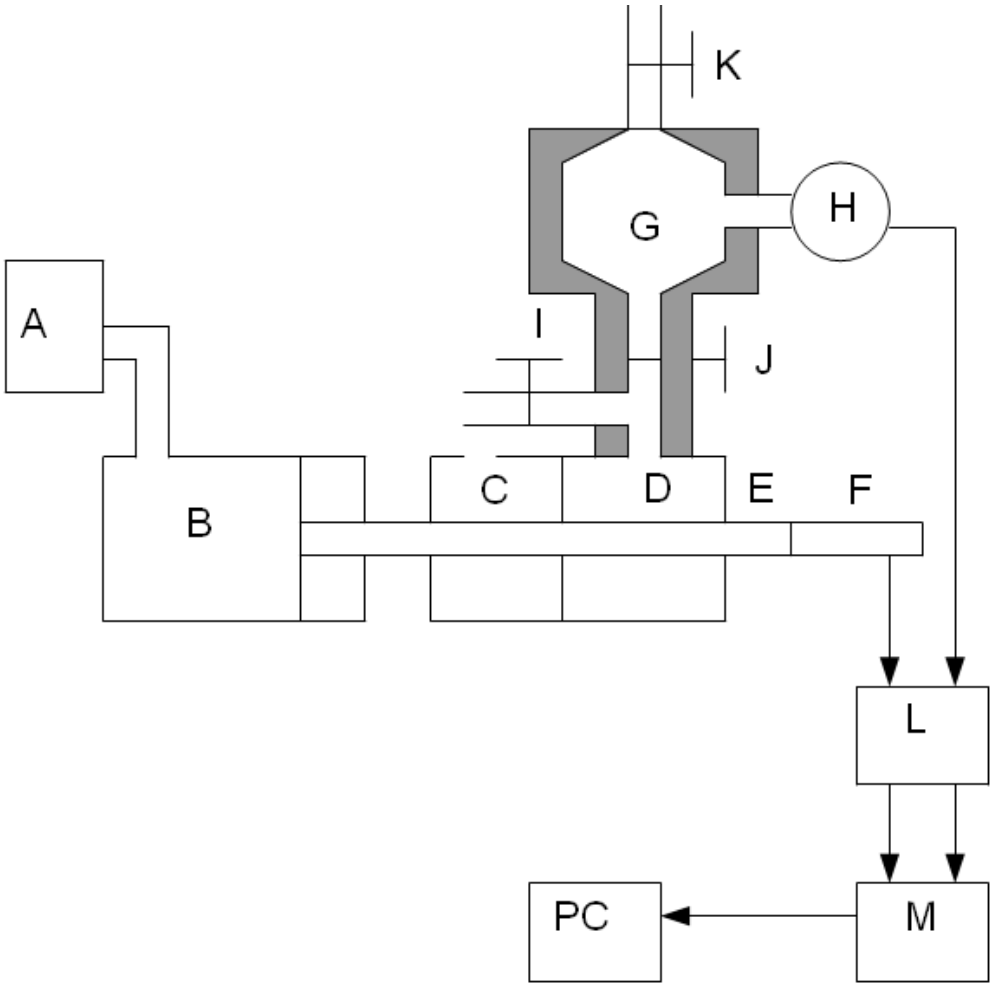

Figure 3.7: A schematic showing the compression device and data acquisition in hydrostatic compression experiments. The letters denote the following components: **A** is the hydraulic pump, **B** is the single action hydraulic cylinder, **C** is the first chamber of the double action hydraulic cylinder connected to ambient pressure, **D** is the 2nd chamber of the double action hydraulic cylinder, **E** is a rod connecting the cylinders and the position sensor, **F** is the position sensor, **G** is the sample chamber, **H** is the pressure sensor, **I**, **J** and **K** are needle valves, **L** is a connection box, **M** is the data acquisition card and **PC** is the computer.

4 Results and Data Analysis

4.1 Error estimates for the initial sample properties

As described in section 3.1, the estimated water content of each patch was calculated from the amount of water added while assuming that all lost mass was due to lost water. Before and after the compression measurements, the water content of each patch of bentonite was measured. These measurements showed that the water content of the bentonite stayed approximately constant during the measurements. The measured water content was higher than the estimated value by approximately 0–0.004 depending on the patch.

Since the possibility of slightly uneven water distribution cannot be ruled out, it was assumed that for all patches with added water, the water content of the patch was 0.002 larger than the estimated value with error $\mathrm{d}\eta = \pm 0.002$. In total five patches of bentonite were made. Their water contents are listed in table 4.1.

After making a sample for the hydrostatic tests, the height and diameter of each sample were measured with a caliper. The uncertainty for both measurements was estimated to be $\pm 0.1\,\mathrm{mm}$, leading to uncertainties $\mathrm{d}h = 0.01\,\mathrm{mm}$ and $\mathrm{d}r = 0.05\,\mathrm{mm}$ for the height and bottom radius, respectively. The uncertainty in the mass of the sample was $\mathrm{d}m = 0.01\,\mathrm{g}$.

These uncertainties were combined using the general formula of error propagation. The obtained error estimate for the volume was $\mathrm{d}V = 0.16\,\mathrm{cm}^3$. The dry density of a sample was calculated from equation (2.15). The application of general formula of error propagation gave the uncertainty $\mathrm{d}\rho_0 = 0.011\,\mathrm{g\,cm}^{-3}$.

Table 4.1: The water content of the patches of bentonite clay. For all patches, the uncertainty is $\mathrm{d}\eta = \pm 0.002$.

Patch number	1	2	3	4	5
Water content η	0.076	0.124	0.166	0.208	0.244

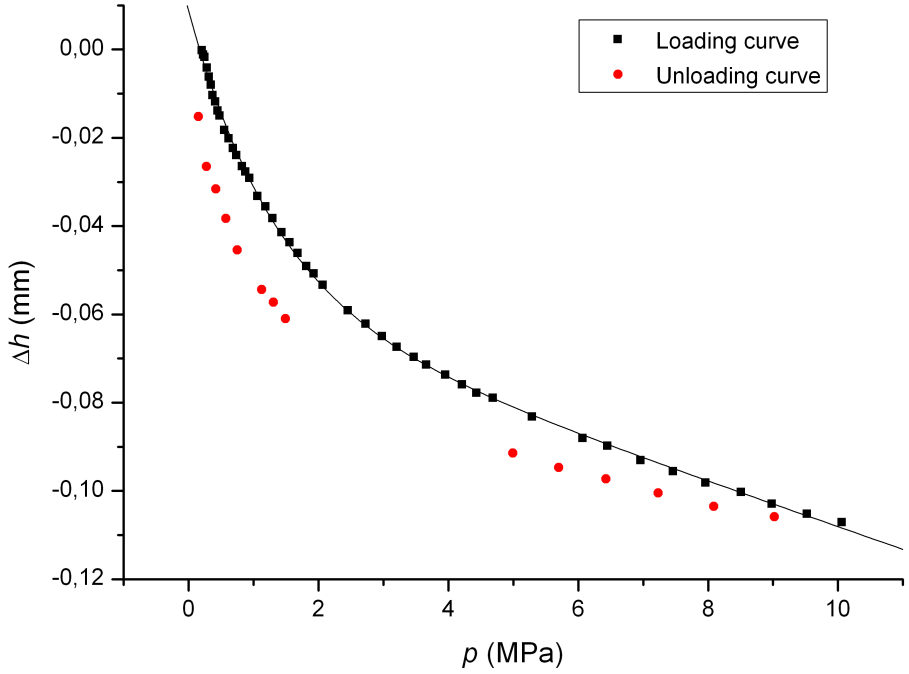

Figure 4.1: The calibration measurement points and the corresponding function fit for the one-dimensional compression device. The calibration function is given in equation (4.1).

4.2 One-dimensional constrained compression

Deformation of the compression device and error estimation

In addition to the bentonite sample, the compression device also undergoes elastic deformation during the experiments. To correct for the deformation of the device, a calibration was made by pressing the sintering surfaces of the device against each other while measuring the position sensor readings as a function of pressure.

The calibration was made by compressing the device from zero to 10 MPa and then returning the pressure back to zero. The calibration was then made by fitting a function by trial and error to the loading part of the

(p,Δh)-curve. (See figure 4.1.) The calibration function thus obtained was

$$\Delta h(p) = a_1 \exp\left(-p/a_2\right) + a_3 + a_4 p \tag{4.1}$$

where

$$\begin{aligned} a_1 &= 0.066\,\mathrm{mm} \\ a_2 &= 1.32\,\mathrm{MPa} \\ a_3 &= -0.057\,\mathrm{mm} \\ a_4 &= -0.0051\,\mathrm{mm\,MPa^{-1}}. \end{aligned}$$

The calibrated sample height values in the bentonite measurements were acquired by subtracting function (4.1) from the measured sample height values. Only the loading part of the loading-unloading curve was used in the determination of the calibration function. This was done to ensure that the calibration would not change the qualitative behavior of the bentonite e.g. by removing some of the actual deformation of the bentonite.

Because the pressure applied to the sample was measured indirectly from the hydraulic pressure (see figure 3.2 on page 13), the choice of the zero level of sample pressure has some ambiguity. The factors that affect the hydraulic pressure include at least friction, the weight of the upper part of the device when it is resting on the hydraulic cylinder, sample pressure and the force exerted by a mechanical spring inside the hydraulic cylinder. Based on observations on the hydraulic pressure, it was estimated that the pressure caused by other factors than sample pressure was $3.0\,\mathrm{bar} \pm 0.5\,\mathrm{bar}$. To ensure that the sintered steel surfaces were properly in contact at the start of the measurement, it was assumed that the sample pressure was zero when the hydraulic pressure was 4.1 bar. This means that the zero sample pressure in the calibration roughly corresponds to actual pressure of $70\,\mathrm{kPa} \pm 30\,\mathrm{kPa}$.

A priori it is not certain that the results obtained in this kind of calibration correspond to the deformation of the device when there is some material between the sintering surfaces. For example if the sintering surfaces are not perfectly parallel, additional compression may occur at the beginning of the compression because the force is not divided equally on the surfaces. For this reason the calibration was checked by compressing different number of discs of copy paper between the sintering surfaces. The measurement was repeated for one to five discs. Then the change in position Δh was plotted as a function of the number of discs N at five constant pressures. The relationship between N and Δh was approximately linear, so the device compression at any pressure could be determined by extrapolating to $N = 0$. The device deformations were measured this way for

pressures 1 MPa, 2 MPa, 3 MPa, 4 MPa and 5 MPa and they agreed very well with the calibration equation (4.1).

Since the objective of the work presented in this thesis is to provide parameters for a simplified numerical model of bentonite deformations, the importance of error estimation of variables is somewhat diminished. Nevertheless it is necessary to provide some crude estimates for the accuracy of the measurements.

The accuracies of the position and pressure sensors were $\mathrm{d}h = \pm 4\,\mu\mathrm{m}$ and $\mathrm{d}p = \pm 0.03\,\mathrm{MPa}$, respectively. From figure 4.1 we see that the calibration error is much greater than the error caused by sensor inaccuracies. From figure 4.1 it can be estimated that if the pressure values are assumed to have no error, the corresponding position values have maximum error of $\pm 0.02\,\mathrm{mm}$. However, the choice of the zero level of the pressure and other experimental uncertainties may increase the error range. It was estimated that if the error in pressure values is omitted, the maximum error in the position values should not exceed $\pm 0.05\,\mathrm{mm}$. It was assumed that the measurement error remained constant in all measurements.

Data analysis

Figure 4.2 shows the measured and calibrated loading curve of a bentonite sample in cyclic one-dimensional compression. The behavior is qualitatively identical with the expected behavior shown in figure 2.2. The approach was to model the virgin curve with some appropriate non-linear function and elastic loops with straight lines corresponding to the linear elasticity theory. The resulting model is depicted in figure 4.3.

The elastic reference sample height at different stages was read from the x-intercepts of the elastic fits, and the yield limits corresponding to this reference height was read from the intersection points of the elastic lines and the virgin curve. By calculating the elastic reference dry densities from the reference height using equation (2.16), it was possible to calculate the p-wave modulus and the yield limit as a function of the dry density at the constant water content of the sample.

The function that was fitted to the measured values of height h and pressure p on the virgin curve were of the form

$$p(h) = a_1 \exp\left(\frac{-h}{a_2}\right) + a_3 + a_4 h, \tag{4.2}$$

where a_i are the parameters of the fit.

The determination of the equations of the straight lines in figure 4.3 is somewhat ambiguous because the observed behavior of the bentonite is

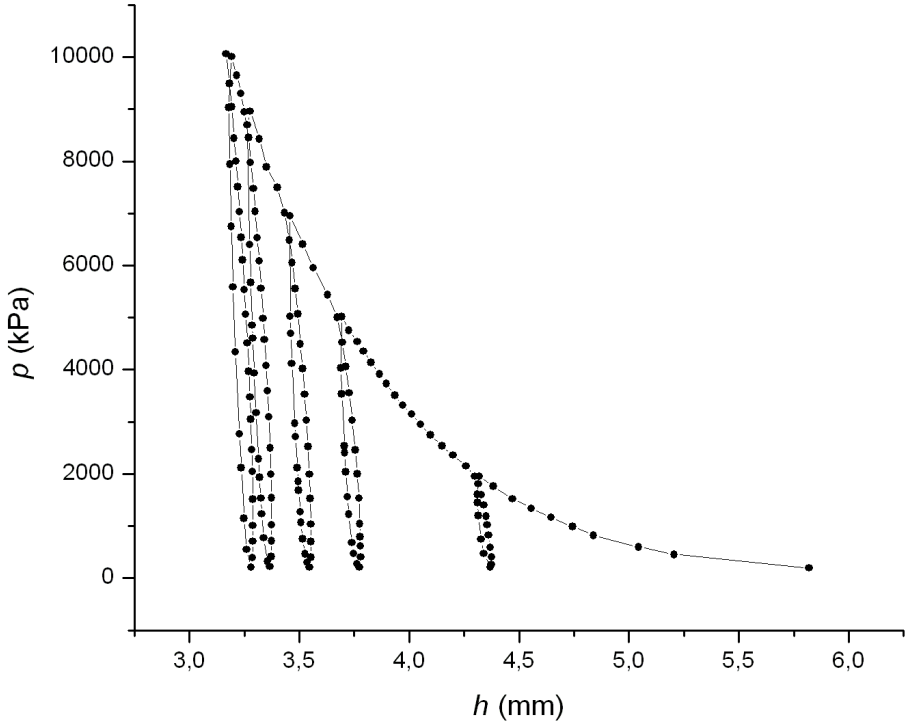

Figure 4.2: The data points for a bentonite sample in one-dimensional constrained compression. The water content and mass of the sample were $\eta = 0.076 \pm 0.002$ and $m = 32.88\,\mathrm{g} \pm 0.02\,\mathrm{g}$, respectively. The lower loops describe elastic deformations and the virgin (shadow) curve describes plastic deformations (see figure 2.2).

not linear. In addition, the accuracy of the device calibration is weakest at low pressures as can been seen from the steep fall in calibration curve in figure 4.1 at low pressures. For these reasons the equations of the lines were determined by selecting two points from the *re-loading part of each loop* in a systematic manner and assuming that the line goes through these points.

The lower points for all but the rightmost loop were chosen from the re-loading part so that the pressure was approximately 1000 kPa. For the rightmost loop the low point was chosen at approximate pressure 500 kPa. The upper points for each loop were chosen from the approximate intersection points of the unloading and re-loading parts of the loop.

Table 4.2 shows the calculated values of the p-wave modulus and yield

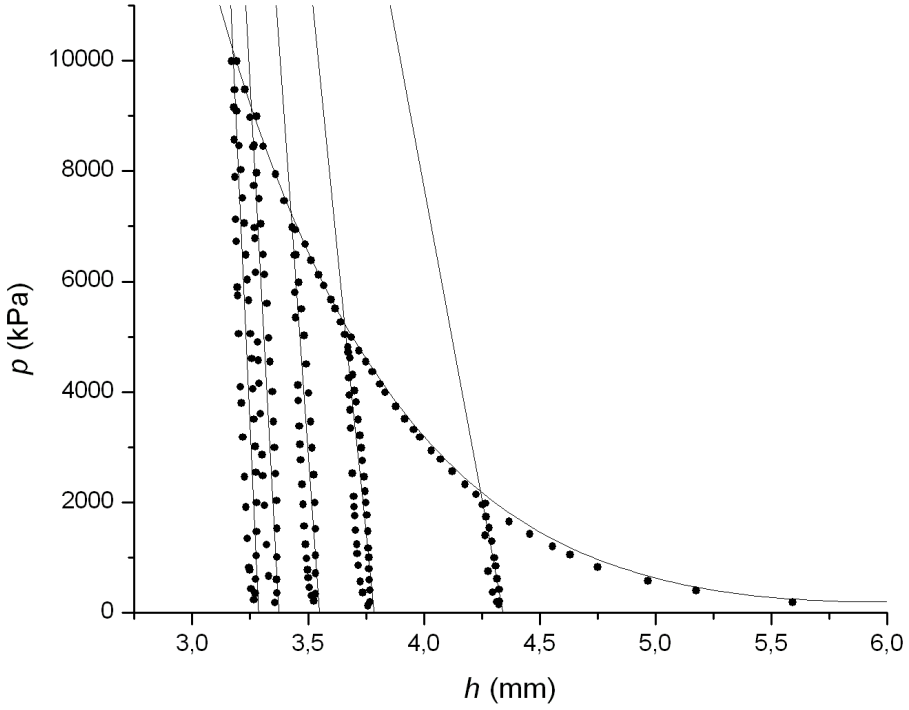

Figure 4.3: The data points, fit of the virgin curve and fits of the elastic regions for the sample in figure 4.2.

limit as a function of the elastic reference dry density obtained from each re-loading section.

The p-wave modulus

By repeating the analysis described in subsection 4.2 for all one-dimensional compression experiments, values for the p-wave modulus at various values of water content η and dry density ρ_0 were obtained. All data points are listed in table A.1 in the appendices.

A non-linear least squares function fit was calculated to provide interpolation estimates for the p-wave modulus for other than measured values of η and ρ_0. The fit thus obtained was

$$M(\rho_0,\eta) = (a + b\eta)\left(\frac{\rho_0}{c - \rho_0}\right) + d, \tag{4.3}$$

Table 4.2: The elastic reference heights, slopes of the lines, elastic reference dry densities, p-wave moduli and yield limits obtained from the linear fits for the elastic parts in figure 4.3. The reference dry densities and p-wave moduli were calculated from the reference height values with equations (2.16) and (2.7), respectively.

Loop number	1	2	3	4	5
$h_{\mathrm{ref}}\,(\mathrm{mm})$	4.35	3.79	3.55	3.38	3.29
$\mathrm{d}p/\mathrm{d}h\,(\mathrm{MPa\,mm^{-1}})$	−22.5	−41.9	−58.7	−76.6	−91.2
$\rho_{0,\mathrm{ref}}\,(\mathrm{g\,cm^{-3}})$	1.117	1.283	1.367	1.438	1.478
$M\,(\mathrm{MPa})$	97.7	159	208	258	300
$p_{\mathrm{yield}}\,(\mathrm{MPa})$	2.20	5.23	7.23	9.13	10.2

where

$$\begin{aligned} a &= 86.4\,\mathrm{MPa} \\ b &= -97.3\,\mathrm{MPa} \\ c &= 1.88\,\mathrm{g\,cm^{-3}} \\ d &= -12.3\,\mathrm{MPa}, \end{aligned}$$

The range used in the interpolation is approximately the trapezoid in (ρ_0,η) -space defined by

$$\begin{aligned} \eta &\in [0.07, 0.25] \\ \rho_0 &\in [1.1\,\mathrm{g\,cm^{-3}}, (1.0 + 1.4\eta)\,\mathrm{g\,cm^{-3}}]. \end{aligned}$$

The data points and the fit (4.3) are shown in figure 4.4.

The yield limit

By repeating the analysis described in subsection 4.2 for all one-dimensional compression experiments, values for the yield limit at different values of water content η and dry density ρ_0 were obtained. All data points are listed in table A.2.

A least squares 2nd order polynomial

$$p_{\mathrm{yield}}(\rho_0,\eta) = a_1 + a_2\rho_0 + a_3\eta + a_4\rho_0^2 + a_5\rho_0\eta + a_6\eta^2, \qquad (4.4)$$

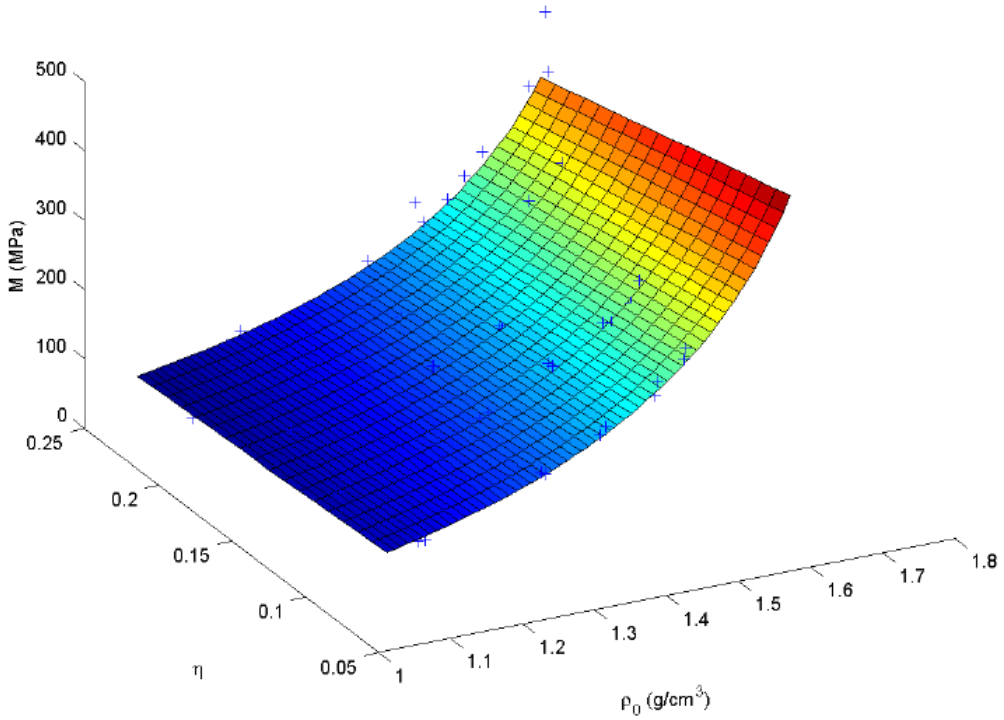

Figure 4.4: The data points and fit (4.3) for the dry density, water content and p-wave modulus according to the one-dimensional measurements.

was fitted to the data points. The values obtained for the coefficients a_i were

$$\begin{aligned} a_1 &= 4.15\,\mathrm{MPa} \\ a_2 &= -25.7\,\mathrm{MPa\,cm^3\,g^{-1}} \\ a_3 &= 84.8\,\mathrm{MPa} \\ a_4 &= 20.3\,\mathrm{MPa\,cm^6\,g^{-2}} \\ a_5 &= -54.8\,\mathrm{MPa\,cm^3\,g^{-1}} \\ a_6 &= -91.4\,\mathrm{MPa}. \end{aligned}$$

The same data range was used in the interpolation of equation (4.4) as with equation (4.3). A graph showing the data points and equation (4.4) is in figure 4.5.

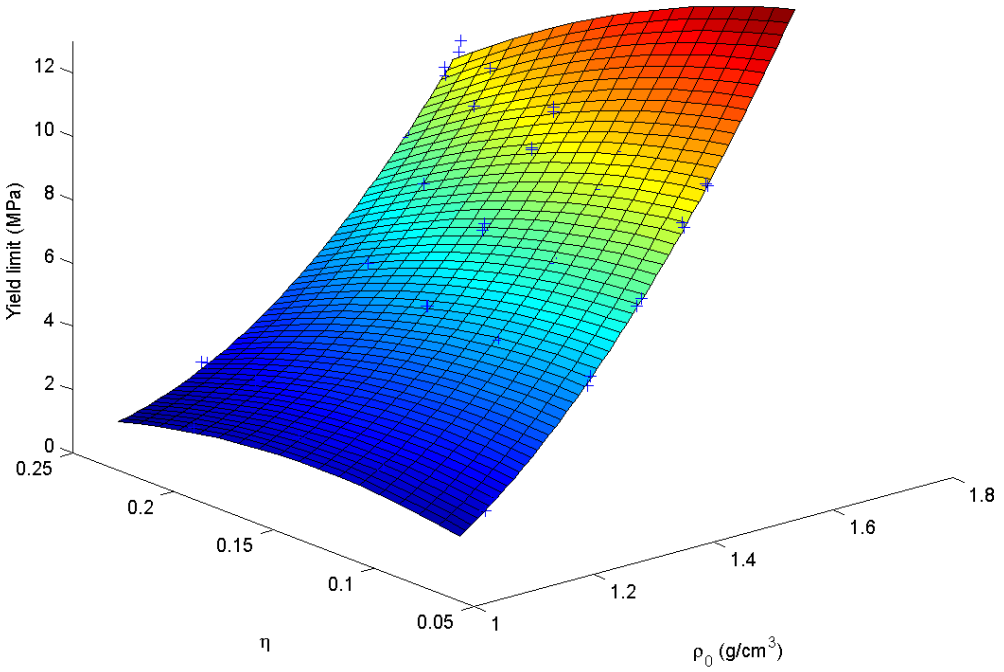

Figure 4.5: The data points and equation (4.4) for the dry density, water content and yield limit according to the one-dimensional compression measurements.

4.3 Hydrostatic compression

Deformation of the compression device and error estimation

Like the one-dimensional compression device, the hydrostatic compression device also experienced deformations during the experiments. As with the one-dimensional experiments, an attempt was made to calibrate the hydrostatic device by pressurizing the water inside the device and measuring the accompanying changes in volume. To take into account the deformation of the rubber cover, a rubber coated steel cylinder with size and shape identical with the clay samples was placed in the compression chamber during the calibration measurements.

This attempt was only partly successful. The volume changes due to the device deformation were roughly repeatable, but the accuracy of the calibration was so weak that it significantly affected the accuracy of the hydrostatic measurements. In addition, from time to time some of the results of individual calibration measurements differed considerably from the rest. Approximately one measurement in four suffered from this anomalous behavior. Because of these complications, the calibration was based on three calibration measurements that agreed approximately with each other as shown in figure 4.6.

The calibration fit for the hydrostatic measurements was obtained by measuring the position sensor reading Δl as a function of pressure and multiplying it with the compressing area of the double action hydraulic cylinder A. The obtained equation was

$$\begin{aligned} \Delta V(p) &= A\Delta l(p) \\ &= A\left(a_1 \exp\left(\frac{-p}{a_2}\right) - a_3 - a_4 p\right), \end{aligned} \tag{4.5}$$

where

$$\begin{aligned} A &= 6.45\,\mathrm{cm}^2 \\ a_1 &= 0.47\,\mathrm{cm} \\ a_2 &= 0.834\,\mathrm{MPa} \\ a_3 &= -0.55\,\mathrm{cm} \\ a_4 &= 0.13\,\mathrm{cm\,MPa}^{-1}. \end{aligned}$$

Figure 4.6 shows that the maximum repeatability uncertainty in the position measurement results was about 0.1 mm, if the error in pressure values

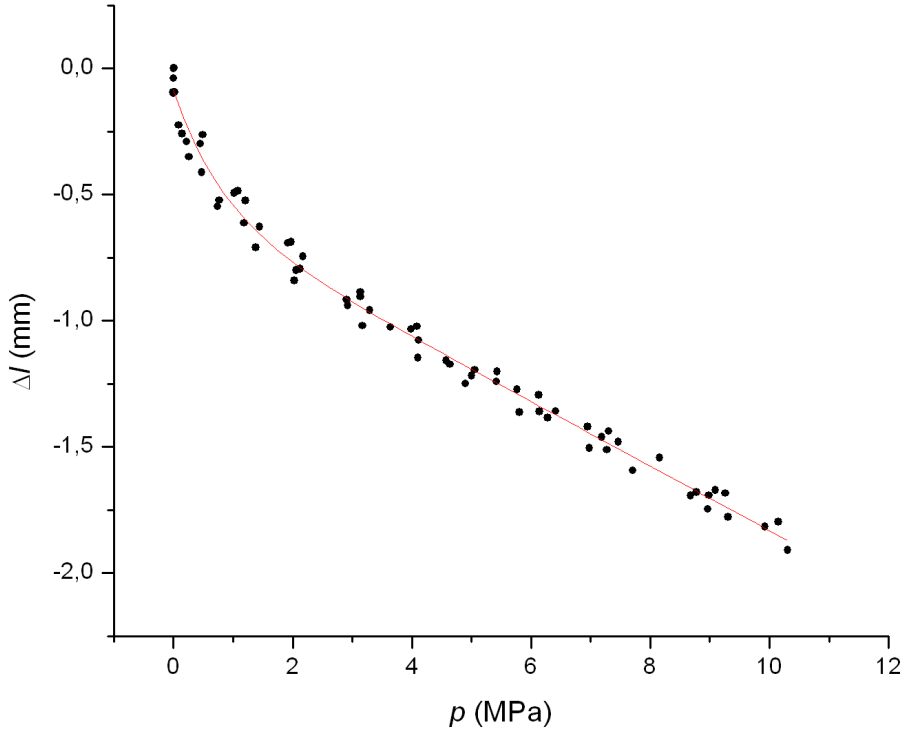

Figure 4.6: The calibration of the hydrostatic device based on three distinct measurements. Each measurements consisted of pressurizing the water to approximately 10 MPa and lowering the pressure back to ambient pressure. The fitted function is in equation (4.5).

is omitted. This corresponds roughly to volume uncertainty of $0.07\,\mathrm{cm}^3$. This is very large compared to the accuracies of the position and pressure sensors, so the errors related sensor accuracies can be omitted. However, the repeatability uncertainty is also very large compared to the measured changes in sample volume (see subsection 4.3), which greatly affects the repeatability of the measurements.

It is currently unclear why the repeatability of the measurements was so poor. A possible explanation was discovered after the measurements were completed and the device was disassembled. Figure 4.7 shows the axis and the piston of the double action hydraulic cylinder together with the piston seal. The large gap between the seal and the edge of its mounting groove means that the insulator can move back and forth as the water is being

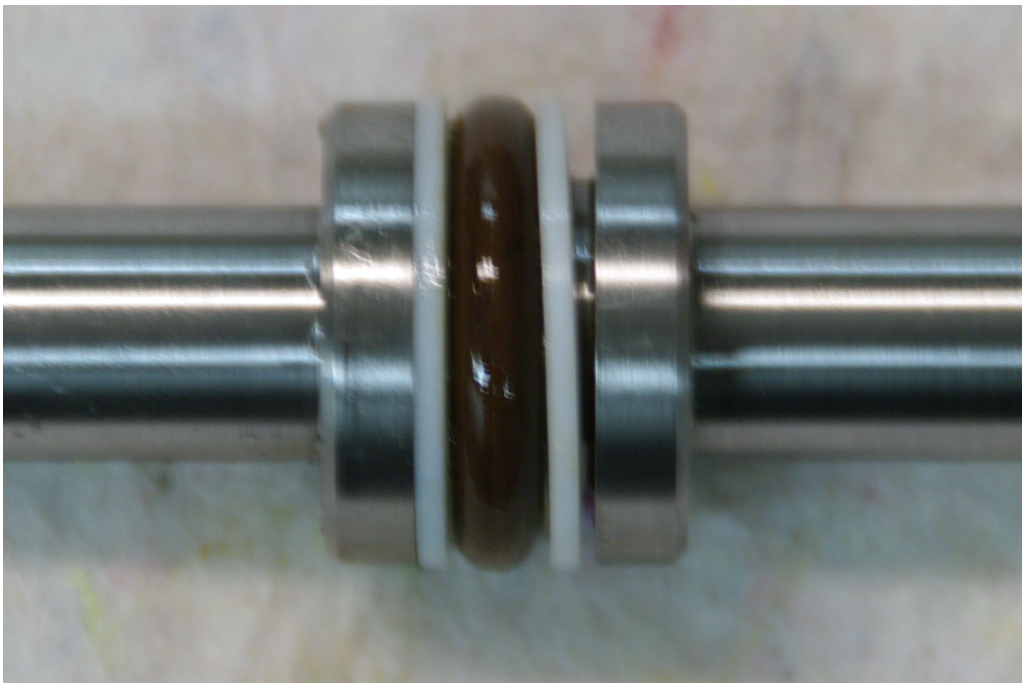

Figure 4.7: A photo showing the axis of the double action hydraulic cylinder after the measurements had been completed. A relatively large gap can be seen between the seals and the edge their mounting groove. This gap allowed the seals to move back and forth during the measurements, possibly causing the poor repeatability.

pressurized and depressurized, possibly resulting in significant changes in the position sensor readings and poor repeatability.

The water inside the hydraulic cylinders contains dissolved air. It is also possible that some of it forms temporary air bubbles when the cylinder is depressurized, causing the poor repeatability.

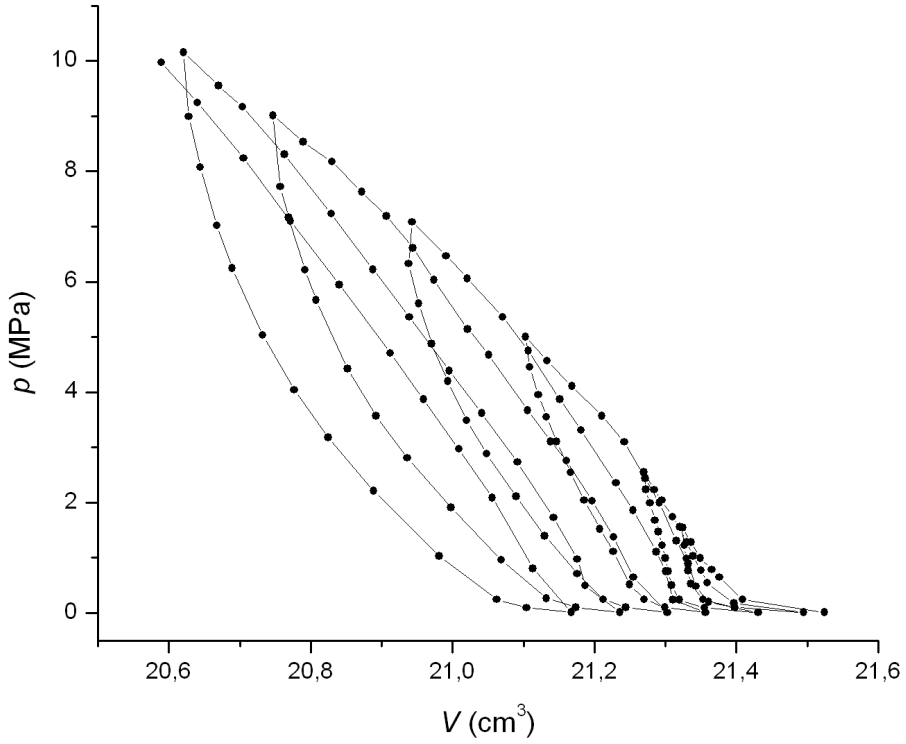

Figure 4.8: The results of a typical hydrostatic compression experiment. This sample has mass $m = 37.80\,\mathrm{g} \pm 0.02\,\mathrm{g}$ and water content $\eta = 0.208 \pm 0.002$.

Data analysis

The original objectives of the analysis of the hydrostatic experiments were analogous to the objectives of the analysis of the one-dimensional experiments (see subsection 4.2). The only difference would have been replacing the height of the sample with the volume, and replacing the p-wave modulus with the bulk modulus. The weak repeatability of the measurements and the unexpectedly small compressibility of the bentonite samples caused large relative error in the hydrostatic measurements, as explained in the next paragraphs.

Figure 4.8 shows a typical example of the results of a hydrostatic measurement. The sample was compressed cyclically with unloading at approximately 1.5 MPa, 2.5 MPa, 5 MPa, 7 MPa, 9 MPa and 10 MPa. Several characteristics should be noted at this point:

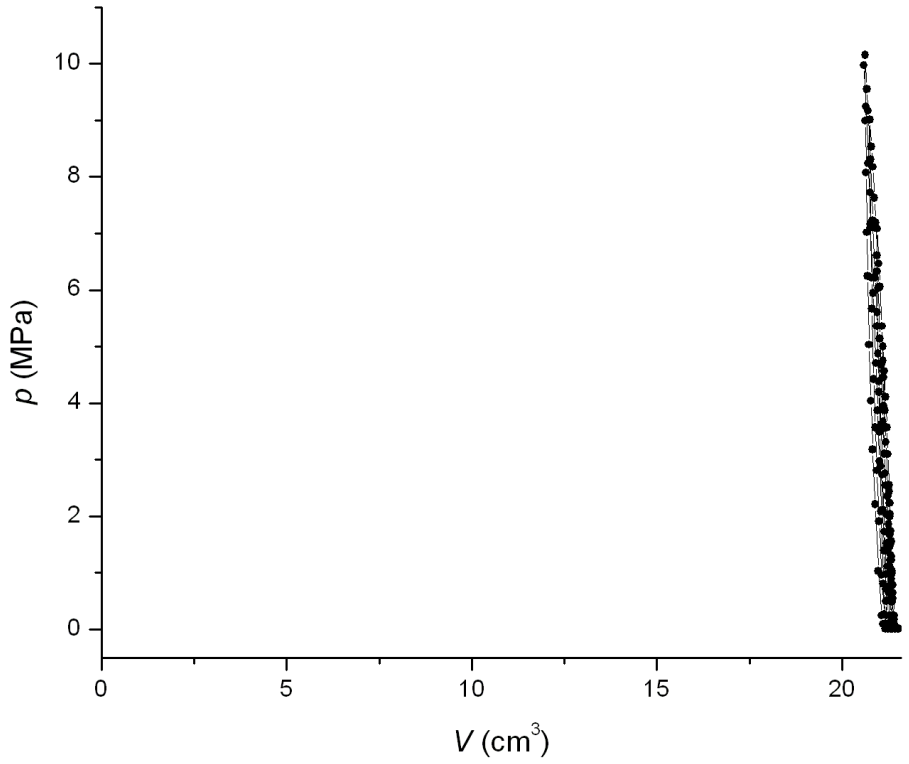

Figure 4.9: Figure 4.8 with different scale on the V-axis. The relative changes in sample volume are very small.

- The plastic deformations are either very small or non-existent, because the sample returns almost to its original volume after compression, as seen in figure 4.9.
- Significant hysteresis, since the unloading and re-loading parts of each elastic loop are significantly apart from each other.
- There is a very steep increase in measured volume as the pressure approaches ambient pressure.

Because no good explanation was found for the steep increase in volume at low pressures, this change was omitted, and all fits were made to the data at higher pressures. As with the one-dimensional experiments, the linear fits were made to the reloading parts of figure 4.8. The first elastic loop (unloading at 1.5 MPa) was not included due to insufficient number of data

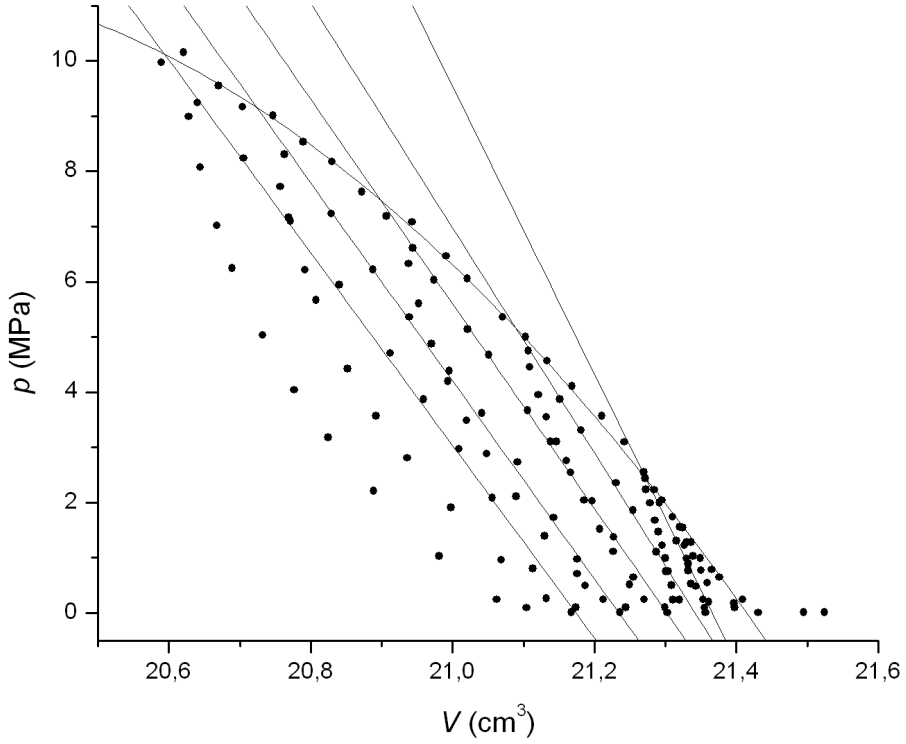

Figure 4.10: The fits for the virgin curve and linear elastic model for the sample in figure 4.8.

points. The virgin curve was modeled as a 2nd order polynomial of volume. The fits obtained this way are shown in figure 4.10. The non-linear part of the re-loading part of each elastic loop has been omitted in the linear fits.

The bulk moduli for the sample in figure 4.8 are in figure 4.11 and table 4.3. According to these measurements, the bulk modulus of bentonite would decrease as its density increases. These results are not sensible and are probably in error. All other measurements were qualitatively similar to the one described here, so there must have been some factors that have greatly distorted the results. See Chapter 5 for further analysis.

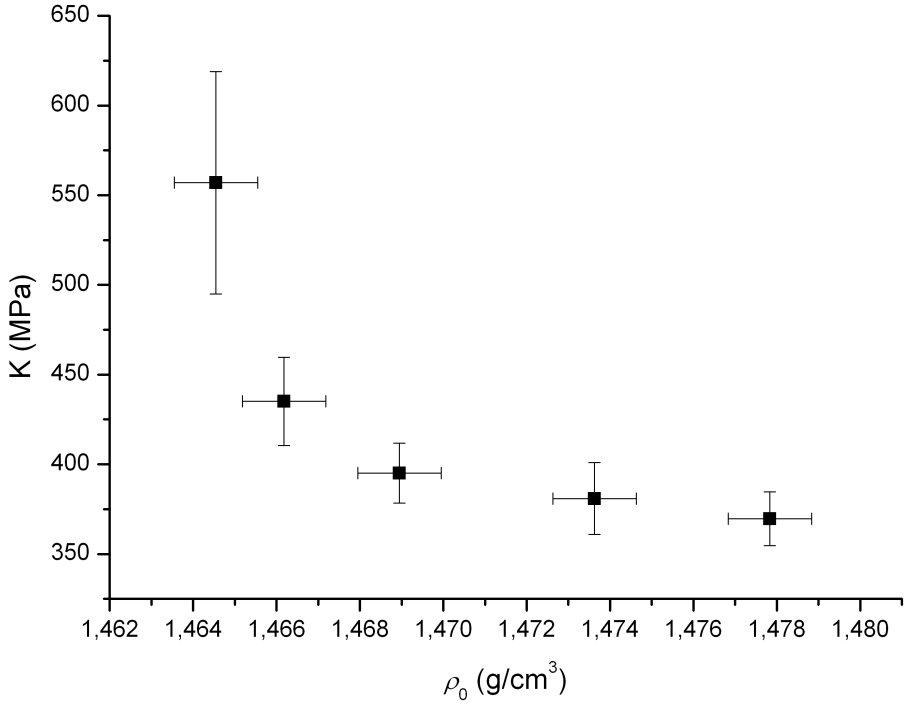

Figure 4.11: The bulk moduli as a function of dry density for the sample in figure 4.8. The bulk modulus error bars are maximum errors calculated from the statistical errors in the parameters of the linear fits in figure 4.10 using maximum-minimum principle. The density error bars were calculated from the accuracy of the position sensor.

The yield limit and the bulk modulus

The observed plastic changes in the volume of all samples in hydrostatic measurements were so small that we cannot be certain that the samples have yielded at all during the measurements. For this reason it is not possible to estimate the hydrostatic yield limit based on these experiments.

As described in subsection 4.8, the results for the bulk moduli were probably in error because the bulk modulus seemed to decrease as density increased. The changes in density were also so small that they fit very well within the error limits of each other, so there is no convincing evidence that the density of the sample actually changed at all. Because of this, it was impossible to draw any meaningful relation between the dry density and

Table 4.3: The elastic reference volumes, slopes of the lines, elastic reference dry densities and bulk moduli obtained from the linear fits for the elastic parts in figure 4.10. The reference dry densities and bulk moduli were calculated from the elastic reference volumes with equations (2.16) and (2.6), respectively.

Loop number	1	2	3	4	5
$V_{\mathrm{ref}}\,(\mathrm{cm}^3)$	21.4	21.3	21.3	21.2	21.2
$\mathrm{d}p/\mathrm{d}V\,(\mathrm{MPa\,cm}^{-3})$	−26.4	−20.4	−18.5	−17.9	−17.5
$\rho_{0,\mathrm{ref}}\,(\mathrm{g\,cm}^{-3})$	1.465	1.466	1.469	1.474	1.478
$K\,(\mathrm{MPa})$	557	435	395	381	370

the bulk modulus. All results for the bulk modulus are in table B.1 in the appendices.

Despite these setbacks, it was possible to calculate estimates for the Poisson ratio and shear modulus from the measured bulk moduli. As seen in figure 4.11, the values of K at the three largest dry density values are quite close to each other. Thus a rough estimate for the bulk modulus at one dry density value can be obtained by taking the average of the last three values for K and assuming that this is the bulk modulus at dry density value determined by the average of the dry density values. For example for the sample in figure 4.11 and table 4.3 the dry density estimate was

$$\begin{aligned}\overline{\rho}_0 &= \frac{\rho_{0,1} + \rho_{0,2} + \rho_{0,3}}{3} \\ &= \frac{1.4690 + 1.4736 + 1.4778}{3}(\mathrm{g\,cm}^{-3}) \\ &\approx 1.487\,\mathrm{g\,cm}^{-3},\end{aligned}$$

Similarly, the estimate for the bulk modulus was

$$\begin{aligned}\overline{K} &= \frac{K_1 + K_2 + K_3}{3} \\ &= \frac{395.02 + 380.94 + 369.58}{3}(\mathrm{MPa}) \\ &\approx 382\,\mathrm{MPa}.\end{aligned}$$

This way it was possible to obtain estimates for the bulk modulus at several dry density and water content values.

All results calculated this way are listed in table 4.4. Table 4.4 also shows the corresponding values for the p-wave modulus calculated with

equation (4.3), as well as the values for the Poisson ratio ν calculated using equation (2.8). Since the Poisson ratio calculated from the hydrostatic and one-dimensional measurements exceeds 1/2 for many samples, it is clear that either the hydrostatic or one-dimensional results are in error. Given the consistency of the one-dimensional measurements and the problems encountered in the hydrostatic measurements, it is very probable that the error is due to defects in the hydrostatic measurements.

Table 4.4: The calculated averages for the dry densities and bulk moduli for all hydrostatic samples. The table also shows the corresponding values for M obtained from equation (4.3) and the values for the Poisson ration ν calculated from the values of M and $\overline{K}$. The fact that for many samples the Poisson ratio exceeds $1/2$ means that something is very probably wrong with the hydrostatic measurements.

η	$\overline{\rho_0}\,(\mathrm{g\,cm^{-3}})$	$\overline{K}\,(\mathrm{MPa})$	$M\,(\mathrm{MPa})$	ν
0.076	1.482	232	284	0.42
0.076	1.497	261	298	0.45
0.076	1.482	239	284	0.43
0.124	1.470	293	256	0.55
0.124	1.474	265	270	0.49
0.124	1.481	282	265	0.52
0.166	1.478	299	247	0.57
0.166	1.485	313	237	0.60
0.166	1.499	335	265	0.58
0.166	1.470	257	241	0.52
0.206	1.474	382	230	0.67
0.206	1.477	384	230	0.67
0.206	1.499	378	250	0.64
0.244	1.498	373	235	0.65
0.244	1.514	404	253	0.65
0.244	1.500	366	233	0.65

4.4 Poisson ratio and shear modulus

The fit (4.3) and the results obtained for the bulk modulus can be used to calculate values for the Poisson ratio of the purified bentonite using equation (2.8). The obtained values were roughly between 0.42 and 0.66 (see table 4.4). As a Poisson ratio at or above 0.5 is not physically meaningful, this lends additional support to the claim that either the one-dimensional or hydrostatic measurements were flawed. Because the one-dimensional compression results were systematic, repeatable and physically sound, it is likely that the error is in the hydrostatic measurements.

Based on the experimental results, it can be estimated that for purified bentonite clay with dry density $\rho_0 \geq 1.47\,\mathrm{g\,cm^{-3}}$ and water content $\eta \in [0.07, 0.25]$ the Poisson ratio ν is

$$0.42 \leq \nu \leq 0.50.$$

The Poisson ratio and the p-wave modulus can be used to calculate the shear modulus G of the purified bentonite by using equation (2.9). The resulting fit is

$$\begin{aligned} G(\rho_0,\eta,\nu) &= \frac{1-2\nu}{2(1-\nu)} M(\rho_0,\eta) \\ &= \frac{1-2\nu}{2(1-\nu)} \left[(a+b\eta) \left(\frac{\rho_0}{c-\rho_0} \right) + d \right], \end{aligned}$$

where

$$\begin{aligned} a &= 86.4\,\mathrm{MPa} \\ b &= -97.3\,\mathrm{MPa} \\ c &= 1.88\,\mathrm{g\,cm^{-3}} \\ d &= -12.3\,\mathrm{MPa}. \end{aligned}$$

The range used in the interpolation is approximately the trapezoid in (ρ_0,η) -space defined by

$$\begin{aligned} \eta &\in [0.07, 0.25] \\ \rho_0 &\in [1.1\,\mathrm{g\,cm^{-3}}, (1.0+1.4\eta)\,\mathrm{g\,cm^{-3}}]. \end{aligned}$$

4.5 Summary

This section summarizes the results for the deformation parameters of purified bentonite clay that were determined in this thesis. For purified bentonite clay with dry density $\rho_0 \geq 1.47\,\mathrm{g\,cm^{-3}}$ and water content $\eta \in [0.07, 0.25]$ the Poisson ratio ν is

$$0.42 \leq \nu \leq 0.50.$$

The fits for the p-wave modulus M and shear modulus G as a function of dry density ρ_0 and water content η are

$$M(\rho_0,\eta) = (a + b\eta)\left(\frac{\rho_0}{c - \rho_0}\right) + d$$

and

$$G(\rho_0,\eta) = \frac{1 - 2\nu}{2(1 - \nu)}\left[(a + b\eta)\left(\frac{\rho_0}{c - \rho_0}\right) + d\right]$$

where the parameters are

$$\begin{aligned} a &= 86.4\,\mathrm{MPa} \\ b &= -97.3\,\mathrm{MPa} \\ c &= 1.88\,\mathrm{g\,cm^{-3}} \\ d &= -12.3\,\mathrm{MPa}. \end{aligned}$$

The functional fit for the yield limit in one-dimensional constrained compression p_{yield} is

$$p_{\mathrm{yield}}(\rho_0,\eta) = a_1 + a_2\rho_0 + a_3\eta + a_4\rho_0^2 + a_5\rho_0\eta + a_6\eta^2,$$

where

$$\begin{aligned} a_1 &= 4.15\,\mathrm{MPa} \\ a_2 &= -25.7\,\mathrm{MPa\,cm^3\,g^{-1}} \\ a_3 &= 84.8\,\mathrm{MPa} \\ a_4 &= 20.3\,\mathrm{MPa\,cm^6\,g^{-2}} \\ a_5 &= -54.8\,\mathrm{MPa\,cm^3\,g^{-1}} \\ a_6 &= -91.4\,\mathrm{MPa}. \end{aligned}$$

In all three cases the data range used in the interpolation is approximately the trapezoid in (ρ_0,η) -space defined by

$$\begin{aligned} \eta &\in [0.07, 0.25] \\ \rho_0 &\in [1.1\,\mathrm{g\,cm^{-3}}, (1.0 + 1.4\eta)\,\mathrm{g\,cm^{-3}}]. \end{aligned}$$

5 Conclusion

The main objective of this thesis was to test and improve experimental methods for measuring the deformation properties of bentonite clay. The secondary objective was to investigate the deformation properties and parameters of purified bentonite clay. This data can be used to validate different deformation models.

The experimental method used in the one-dimensional constrained compression experiments works well within the pressure range 0–10 MPa. In the future, this method can be used to measure elasto-plastic deformation properties of different bentonite samples. The only weakness is that increasing the maximum pressure from the present 10 MPa may not be possible with the current device, should such large pressures be necessary.

The hydrostatic compression experiments were not very successful due to the unexpectedly high hydrostatic yield limit of the purified bentonite with dry density $\rho_0 \approx 1.48\,\mathrm{g\,cm^{-3}}$. Because of the high yield limit, it was not possible to cause significant plastic deformations in hydrostatic compression. Another factor was the unexpectedly low repeatability of the hydrostatic measurements as discussed in section 4.3. The principle used in the measurements has previously been shown to work for unpurified bentonite. [7]

The structure of the mounting groove of the piston seal of one of the hydraulic cylinders was probably one of the reasons for the low accuracy. This structural property should be relatively easy to fix in the future. It is therefore possible that with some improvements the present compression device can be used to investigate the deformation properties of bentonite of this type and density in hydrostatic compression. It is probable that the hydrostatic compression device can be used to measure the properties of purified bentonite also, but at lower dry density values than are presented in this thesis, because the changes in sample volume would likely be larger for less dense bentonite. It should also be possible to use the present device to measure the hydrostatic deformation parameters of unpurified bentonite, because previous work has shown that unpurified MX-80 bentonite has a much lower hydrostatic yield limit than the purified bentonite studied here. [7]

Functional fits for several deformation parameters of purified bentonite clay were calculated from the measured data. These results are summarized in section 4.5 on page 40. The summary includes

- functional fits for the p-wave modulus and one-dimensional constrained compression yield limit as a function of bentonite density and water

content

- an estimate for the Poisson ratio
- a functional fit for the shear modulus based on the p-wave modulus fit and Poisson ratio estimate.

Appendices

A Measured values for p-wave modulus and yield limit in one-dimensional experiments

B Measured values for bulk modulus

Bibliography

[1] Posiva Oy. Safe final disposal of spent nuclear fuel. Brochure, 2011. Also available online at `http://www.posiva.fi/files/1233/Posiva_final_disposal_en.pdf`. Cited on May 15, 2012.

[2] Jacob Lubliner. *Plasticity Theory*. Dover Publications Inc, 2008.

[3] David Muir Wood. *Soil Behaviour and Critical State Soil Mechanics*. Cambridge University Press, 1990.

[4] L. D. Landau and E. M. Lifshitz. *Theory of Elasticity*. Pergamon Press, 1959.

[5] Mary L. Boas. *Mathematical Methods in the Physical Sciences*. John Wiley & Sons Inc, third edition, 2006.

[6] L. M. Kachanov. *Fundamentals of the Theory of Plasticity*. Dover Publications Inc, 2004.

[7] Aaro Eloranta. Mittausmenetelmä bentoniitin muodonmuutosten tutkimiseen hydrostaattisessa puristuksessa. Research training report, University of Jyväskylä, 2010.

A Measured values for p-wave modulus and yield limit in one-dimensional experiments

Tables A.1 and A.2 show all data points of the p-wave modulus and yield limit, respectively, in the one-dimensional constrained compression measurements.

Table A.1: All measurement points of the dry density ρ_0, water content η and p-wave modulus M in one-dimensional compression experiments.

$\rho_0\,(\mathrm{g\,cm^{-3}})$	η	M (MPa)	$\rho_0\,(\mathrm{g\,cm^{-3}})$	η	M (MPa)
1.106	0.076	98.4	1.486	0.166	246
1.278	0.076	163	1.523	0.166	258
1.360	0.076	198	1.143	0.208	76.6
1.436	0.076	239	1.377	0.208	160
1.476	0.076	283	1.488	0.208	212
1.117	0.076	97.7	1.576	0.208	331
1.283	0.076	159	1.613	0.208	343
1.367	0.076	208	1.063	0.208	69.3
1.438	0.076	258	1.165	0.208	85.3
1.478	0.076	300	1.353	0.208	155
1.098	0.124	77.1	1.447	0.208	202
1.304	0.124	165	1.531	0.208	286
1.392	0.124	213	1.557	0.208	260
1.474	0.124	259	1.205	0.244	108
1.513	0.124	312	1.457	0.244	213
1.096	0.124	91.9	1.540	0.244	297
1.290	0.124	158	1.604	0.244	378
1.386	0.124	219	1.626	0.244	481
1.462	0.124	261	1.183	0.244	93.2
1.501	0.124	282	1.379	0.244	174
1.115	0.166	110	1.446	0.244	243
1.312	0.166	161	1.491	0.244	240
1.404	0.166	201	1.515	0.244	267
1.486	0.166	232	1.195	0.244	86.2
1.523	0.166	257	1.446	0.244	167
1.098	0.166	72.0	1.543	0.244	254
1.311	0.166	162	1.602	0.244	311
1.407	0.166	197	1.630	0.244	395

Table A.2: All measurement points of the dry density ρ_0, water content η and yield limit p_{yield} in one-dimensional compression experiments.

$\rho_0\,(\mathrm{g\,cm^{-3}})$	η	$p_{\text{yield}}\,(\mathrm{MPa})$	$\rho_0\,(\mathrm{g\,cm^{-3}})$	η	$p_{\text{yield}}\,(\mathrm{MPa})$
1.106	0.076	1.88	1.311	0.166	5.10
1.278	0.076	4.94	1.407	0.166	7.21
1.360	0.076	7.03	1.486	0.166	9.21
1.436	0.076	9.28	1.523	0.166	10.3
1.476	0.076	10.3	1.143	0.208	1.16
1.117	0.076	2.21	1.377	0.208	4.44
1.283	0.076	5.23	1.488	0.208	6.88
1.367	0.076	7.23	1.576	0.208	8.76
1.438	0.076	9.13	1.613	0.208	9.92
1.478	0.076	10.2	1.063	0.208	1.50
1.098	0.124	1.98	1.165	0.208	2.45
1.304	0.124	5.17	1.353	0.208	5.21
1.392	0.124	7.11	1.447	0.208	7.23
1.474	0.124	9.15	1.531	0.208	9.28
1.513	0.124	10.1	1.557	0.208	10.3
1.096	0.124	2.05	1.205	0.244	1.97
1.290	0.124	5.14	1.457	0.244	5.16
1.386	0.124	7.10	1.540	0.244	7.05
1.462	0.124	9.04	1.604	0.244	8.99
1.501	0.124	10.0	1.626	0.244	9.61
1.115	0.166	2.09	1.195	0.244	2.01
1.312	0.166	5.10	1.446	0.244	5.10
1.404	0.166	7.03	1.543	0.244	7.34
1.486	0.166	9.14	1.602	0.244	9.27
1.523	0.166	10.2	1.630	0.244	9.96
1.098	0.166	2.02			

B Measured values for bulk modulus

Table B.1 shows all results for the bulk modulus at different dry density and water content values. The results are likely in error, because the bulk modulus seems to decrease as density increases, which makes no sense in terms of physics. For further information, see section 4.3.

Table B.1: All measurement points of the dry density ρ_0, water content η and bulk modulus K in hydrostatic compression experiments.

$\rho_0\,(\mathrm{g\,cm^{-3}})$	η	K (MPa)	$\rho_0\,(\mathrm{g\,cm^{-3}})$	η	K (MPa)
1.470	0.076	308	1.493	0.166	393
1.471	0.076	253	1.495	0.166	352
1.475	0.076	234	1.498	0.166	326
1.482	0.076	230	1.503	0.166	326
1.489	0.076	233	1.457	0.166	282
1.492	0.076	274	1.460	0.166	253
1.497	0.076	258	1.469	0.166	253
1.497	0.076	264	1.478	0.166	264
1.502	0.076	263	1.465	0.208	557
1.471	0.076	253	1.466	0.208	435
1.475	0.076	238	1.469	0.208	395
1.482	0.076	237	1.474	0.208	381
1.489	0.076	241	1.478	0.208	370
1.464	0.124	489	1.472	0.208	454
1.463	0.124	335	1.473	0.208	395
1.465	0.124	300	1.478	0.208	386
1.470	0.124	291	1.481	0.208	371
1.475	0.124	287	1.481	0.208	412
1.463	0.124	297	1.492	0.208	397
1.466	0.124	267	1.195	0.208	375
1.474	0.124	262	1.503	0.208	367
1.481	0.124	266	1.487	0.244	768
1.470	0.124	310	1.488	0.244	437
1.473	0.124	282	1.491	0.244	379
1.481	0.124	278	1.498	0.244	358
1.488	0.124	290	1.506	0.244	384
1.472	0.166	639	1.503	0.244	450
1.471	0.166	348	1.507	0.244	395
1.473	0.166	310	1.514	0.244	395
1.477	0.166	292	1.521	0.244	421
1.483	0.166	297	1.482	0.244	415
1.478	0.166	373	1.487	0.244	358
1.480	0.166	323	1.496	0.244	353
1.484	0.166	305	1.506	0.244	387
1.490	0.166	311			